Journal of Alloys and Compounds 1037 (2025) 182271

Contents lists available at ScienceDirect

Journal of Alloys and Compounds

journal homepage: www.elsevier.com/locate/jalcom

Evaluation of manganese chromium metal organic framework and cobalt nickel iron layered double hydroxide composite synthesised by electrodeposition for supercapacitor applications

Gift Rutavi [*], Delvina Japhet Tarimo, Vusani Muswa Maphiri, Vianney Ngoyi Kitenge, Kabir Opeyemi Otun, Hellen Ngunya Mutua, Ncholu Manyala [*]

Department of Physics, SARChI in Nano Materials for Energy storage and Water purification applications, University of Pretoria, 0028, South Africa

ARTICLE INFO

Keywords:
Metal organic frameworks
Layered double hydroxides
Galvanostatic electrodeposition
Specific energy
Capacity retention

ABSTRACT

Chronopotentiometry electrodeposition was used to synthesize manganese chromite metal organic framework (MnCr-MOF- τ) on nickel foam (NF) where τ represents, the duration of the electrodeposition time in minutes. The same procedure was used to deposit cobalt nickel iron layered double hydroxide (CoNiFe-LDH) on MnCr-MOF-20 min to form the MOF-20 min @ CoNiFe-LDH. The synergetic effect of the highly porous MOF with a metal centre and branches with enhanced conductivity increases the performance of the composite. The high reversible redox kinetics of the LDH endowed the composite electrode with high electrochemical performance. The electrode yielded a specific capacity of 296 ± 5 mAh g^{-1} at a specific current of 0.5 A g^{-1} in a 3-electrode set-up with a high-capacity retention of 70.4 % after 5, 000 galvanostatic charge discharge (GCD) cycles in 2 M KOH electrolyte. The composite was incorporated into a supercapacitor device with activated carbon from Amarula husk (AMH) as the negative electrode. The fabricated MOF-20 min @ CoNiFe-LDH//AMH device produced a high electrochemical performance in a 2-electrode set-up with a specific energy of 76.6 ± 0.5 Wh kg^{-1} at a specific power of 724.9 ± 0.5 W kg^{-1}. The device also showed great stability with a capacity retention of 81.2 ± 0.5 % after 10, 000 GCD cycles at 10 A g^{-1}.

1. Introduction

There is an urgent need to revolutionise energy storage systems to facilitate the shift from hazardous fossil fuels to renewable energy sources [1–4]. Supercapacitors offer some favourable attributes that lead them to be favoured in replacing or complementing lithium-ion batteries (LIBs). These include a larger specific power, longer cycling life, and faster charge-discharge compared to LIBs [5–8]. Among the components of a supercapacitor, the electrode has a significant contribution to the overall electrochemical performance of the supercapacitor device [9,10].

Metal organic frameworks (MOF) which are crystalline materials built from inorganic metal ions and organic linkers have been investigated intensively for supercapacitor applications as positive electrodes [11]. This is due to their high specific capacity which is attributed to their porosity permitting ion access, large specific surface area, and huge regions of transitional metal sites accessible to electrolyte ions which become redox active sites for electrochemical reactions [12–14]. Bimetallic MOF are known to possess more favourable features compared to monometallic MOF due to the enhanced electronic conductivity and high redox activity introduced by the availing of a different metal centre and collaborative benefits of two different metals in the MOF nanostructures [15–18]. However, MOFs suffer from poor electrical conductivity, poor rate performance and poor chemical stability which hinder their use as electrode material for supercapacitor applications [19,20]. This can be alleviated by either using MOF derivatives or MOF composites. The latter has advantages like better electron conduction and mild synthesis which retains microstructure such as the pore structure for ion diffusion [21,22]. Layered double hydroxides (LDH) are favourable candidates for constructing MOF composites due to their layered structure suitable for shorter diffusion distances, the availability of metal cations with a range of oxidation states and the availability of many redox active sites [23,24]. Fangqi Ye et. al epitaxially deposited NiCo-LDH nanowrinkles onto Co-MOF, and the synthesized Co-MOF@NiCo-LDH composite which yielded an enormous areal capacitance of 44.1 F cm^{-2} at current density of

---

[*] Corresponding authors.
E-mail addresses: rutavigift@yahoo.com (G. Rutavi), ncholu.manyala@up.ac.za (N. Manyala).

https://doi.org/10.1016/j.jallcom.2025.182271
Received 26 April 2025; Received in revised form 11 July 2025; Accepted 14 July 2025

5 mA cm^{-2} compared to 17.0 F cm^{-2} for the pristine Co-MOF [21]. Wenwen Zheng et. al used in-situ nucleation to grow Ni-MOF/S on NiAl-LDH, and the composite NiAl-LDH/ Ni-MOF/S produced a high specific capacitance of 1670 F g^{-1} at 1 A g^{-1} compared to 1140 F g^{-1} for Ni-MOF [25].

The synthesis method is a principal factor to be considered when fabricating an electrode as it affects features such as the dimensionality, specific surface area and architecture of the electrode material which in turn influence the charge-discharge process [26]. The electrodeposition route benefits from excluding insulating polymeric binders which makes it important to add conducting additives to compensate for the loss in electric conductivities. Additionally, it is easy to regulate the desired features of the electrode materials such as thickness and morphology by adjusting parameters such as solution concentration, deposition time duration, voltage and current [27–30]. For example, Hamed Soltani et.al observed a significant variance in the specific capacitance of g-C_3N_4/MnO_2 for three electrodes electrodeposited with a duration of 1, 2 and 3 min, yielding a specific capacitance of 87.6, 67.0 and 49.5 F g^{-1} at 0.5 A g^{-1}, respectively. The drop in the specific capacitance with deposition time was attributed to the rise in the MnO_2 thickness leading to a decrease of the amount of active materials per unit area and the specific area, this occurs since the majority of the electrochemical reactions take place on the surface [31].

In this work, chronopotentiometry electrodeposition was performed twice, first to electrodeposit MnCr-MOF-τ, on nickel foam substrate where τ is the electrodeposition time whose values are 10, 20 and 30 min. The deposition time of 20 min yielded the best electrochemical performance in 2 M KOH electrolyte and therefore CoNiFe-LDH was electrodeposited on it to form the MOF-20 min @ CoNiFe-LDH composite electrode. This electrode yielded a high specific capacity of 296 mAh g^{-1}. A supercapacitor device, MOF-20 min @ CoNiFe-LDH//AMH was then assembled with CoNiFe-LDH electrode as the positive electrode and activated carbon from Amarula husk (AMH) as the negative electrode in 2 M KOH. The device produced a great electrochemical performance with a specific energy of 76.6 ± 0.5 Wh kg^{-1} corresponding to a specific power of 724.9 W ± 0.5 kg^{-1} at 1 A g^{-1}. The cycling stability of the device was incredibly good with capacity retention of 81.0 ± 0.5 % after 10,000 constant GCD cycles at 10 A g^{-1}. The high performance of the device can be credited to the synergetic effect of LDH and the MOF with the enhanced electrical conductivity provided by the introduction of the carbon material in the device resulting in a large specific capacity aided by the electrodeposition synthesis which ensured robust contact with the current collector.

2. Experimental section

2.1. Materials

The chemicals were without further purification. Deionised water [DW] was purified using the DRAWELL purification machine, and NF was purchased from Alantum (Munich, Germany). Manganese acetate hexahydrate [$Mn(CH_3CO_2)_2{\cdot}4H_2O$] (purity ≥ 99 %), chromium(III) potassium sulphate dodecahydrate [$KCr_2(SO_4){\cdot}12H_2O$] (purity ≥ 99 %), sodium sulphate [Na_2SO_4] (purity ≥ 99 %), cobalt nitrate hexahydrate [$Co(NO_3)_2{\bullet}6H_2O$] (purity ≥ 99 %), nickel nitrate hexahydrate [$Ni(NO_3)_2{\bullet}6H_2O$] (purity ≥ 99 %) and iron III nitrate nonahydrate [$Fe(NO_3)_3{\bullet}9H_2O$] (purity ≥ 99 %) were all purchased from Merck (Johannesburg). Hydrochloric acid [HCl], ethanol [CH_3CH_2OH] (purity99.9 %) (purity32 %), and acetone [$(CH_3)_2CO$] (purity > 99 %) were acquired from (Sigma Aldrich, Steinheim, Germany). 1-Methylimidazole (1-MIM) and 2-Methylimidazole (2-MIM) were purchased from LABCHEM (Johannesburg, South Africa).

2.2. Preparation of NF substrate

The chemical cleaning of NF followed the procedure covered in our previous work [23]. The purchased NF when exposed to damp humid air, tends to form an inert hydroxide/oxide layer, this cleansing procedure is meant to remove this layer. Briefly, a 2 cm× 1 cm NF piece was successively dipped for 20 min in 1 M HCl, followed by acetone, then ethanol and finally DW. The cleaned piece was then dried for 12 h in an oven at 60° C.

2.3. Preparation of MnCr-MOF-τ on NF

Solution A was prepared by immersing 0.03 M of (1-MIM) and 0.06 M of (2-MIM) in 100 mL of DW. The solution was stirred for 45 min at room temperature using a magnetic stirrer. Solution B was prepared by adding 0.01 M $Mn(CH_3CO_2)_2{\cdot}4H_2O$ and 0.01 M of $KCr_2(SO_4)_2{\cdot}12H_2O$ into 100 mL of DW. This solution was then stirred for 45 min at room temperature.

The two solutions were then mixed and stirred again for 30 min to produce solution C. Room temperature chronopotentiometry electrodeposition was used by applying a constant current density of 10 mA cm^{-2} for 10 min in a three-electrode set-up using the Bio-Logic workstation with chemically cleaned NF, platinum wire and Ag/AgCl as the working electrode (WE), counter electrode (CE), and reference electrode (RE), respectively in solution C. The electrode was then rinsed in DW and dried in the oven at 60° C for 12 h. The procedure was repeated for 20 and 30 min and the electrodes were labelled as MnCr-MOF-10 min, MnCr-MOF-20 min, and MnCr-MOF-30 min with electrode mass loadings of 0.6, 1.0 and 1.3 ± 0.1 g cm^{-2} respectively.

2.4. Synthesis of CoNiFe-LDH, MOF-20 min @ CoNiFe-LDH and AMH

CoNiFe-LDH was grown directly on NF following this procedure: 0.01 M of Co $(NO_3)_2{\bullet}6H_2O$, 0.01 M of Ni $(NO_3)_2{\bullet}6H_2O$ and 0.01 M of Fe $(NO_3)_3{\bullet}9H_2O$ were added into 500 mL of DW. The mixture was stirred using a magnetic stirrer for 45 min before it was taken for the electrodeposition using the procedure described in Section 2.3 but with the CE, RE and WE dipped in this solution in place of solution C. The electrode was labelled as CoNiFe-LDH.

To synthesise the composite electrode, MOF-20 min @ CoNiFe-LDH, this procedure was repeated but with MnCr-MOF-20 min being used as the WE instead of NF. The synthesis of MOF-20 min @ CoNiFe-LDH is illustrated in Scheme 1. AMH was synthesized following our previous work [32]. The mass loadings of CoNiFe-LDH, MOF-20 min @ CoNiFe-LDH and AMH 1.0, 1.9 and 6.0 ± 0.1 cm^{-2} respectively.

2.5. Material characterisation

The Zeiss ULTRA PLUS FEG-SEM (Akishima-Shi, Japan), which also contains an energy-dispersive X-ray spectroscopy was employed to obtain the morphology and elemental composition of MnCr-MOF-20 min, CoNiFe-LDH and MOF-20 min @ CoNiFe-LDH electrodes. The transition electron microscopy (TEM) images were acquired using the JEOL JEM 2100 F operating at 1.0 kV. The device operates with an accelerating voltage of 2.0 kV. The WITec alpha-300 RAS+ confocal micro-Raman microscope (Focus Innovations, Ulm Germany) was used to perform the Raman analysis of the electrodes. The measurements were conducted using a 532 nm laser at a power of 5 ± 0.3 mW, with a spectral acquisition of 450 s using a 50X objective.

2.6. Electrochemical characterisation

The measurement of the electrochemical performance of the electrodes was done using the Bio-Logic workstation potentiostat. In a 3-electrode set-up, the RE and CE operated as stated in Section 2.3 while the WE were MnCr-MOF-τ, CoNiFe-LDH, and MOF-20 min @ CoNiFe-LDH. GCD, cyclic voltammetry (CV) and Potentiostatic electrochemical impedance spectroscopy (EIS) were all performed in 2 M KOH for both the half and full-cell configuration. This was performed using an

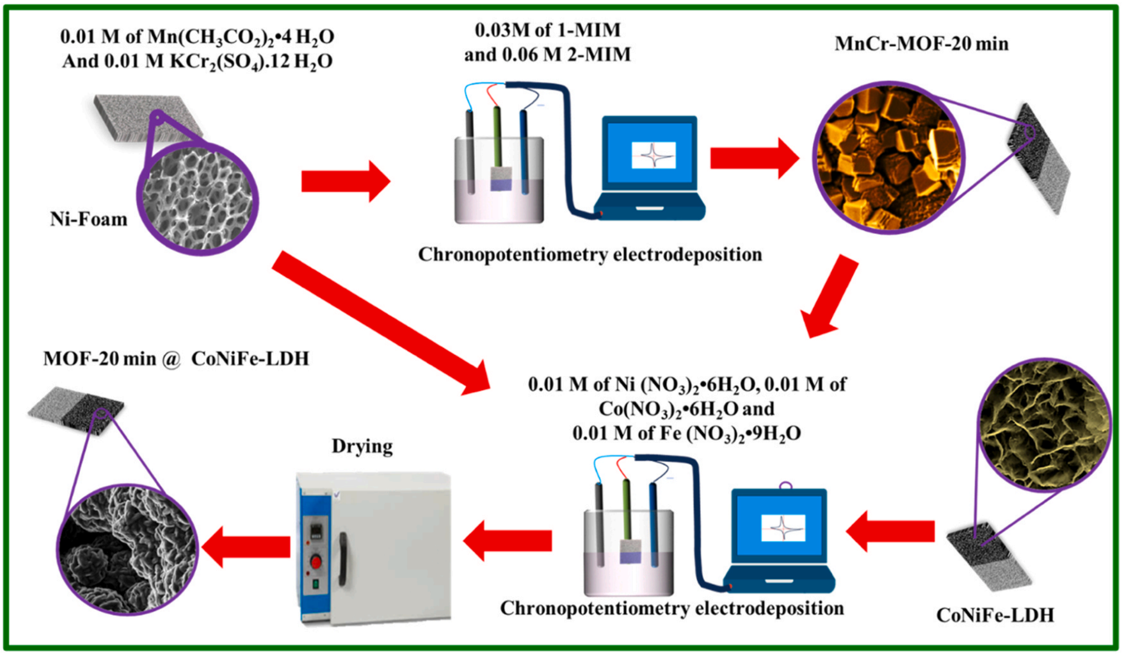

Scheme 1. Schematic illustration of the synthesis of MOF-20 min @ CoNiFe-LDH electrode.

alternating voltage of 10 mV, the frequency range was from 100 kHz to 10 mHz.

3. Results and analysis

3.1. Microstructural characterisation and analysis

Fig. 1 shows the SEM micrograms of MnCr-MOF-τ, Fig. 1(a) shows the sparsely grown octahedral crystals of MnCr-MOF-10 min with an average diameter (d ≈ 100 ± 5nm), as the electrodeposition time increases, the nanocrystals group together as shown in MnCr-MOF-20 min in Fig. 1(b). This arrangement displays enhanced porosity and increased pathways for ion transport. In Fig. 1(c), the nanocrystals have merged with increased thickness, collapsing the octahedral arrangement.

Fig. 2 shows the SEM images of MnCr-MOF-20 min, CoNiFe-LDH, and MOF-20 min @ CoNiFe-LDH. In Fig. 2(a) and (b), the MnCr-MOF-20 min images at low and high-magnification show octahedral structure with a distribution that can permit ion transport. This is consistent with some reported morphology for MOFs [33]. In Fig. 2(c) and (d), the CoNiFe-LDH images at low and high resolution show some nanosheets. The structure provides channels for ion diffusion. Fig (e) and (f) show the micrograms of MOF-20 min @ CoNiFe-LDH at low and high resolution. The morphology shows the LDH nanosheets wrapped around the MnCr-MOF-20 min nanostructures. The amalgamation of the nanosheets and octahedral nanostructure increases revealing more sites for both adsorption and mobility of ions.

Fig. 2(g-n) EDS mapping of MOF-20 min@ CoNiFe-LDH, showing the elements of the MOF and LDH evenly distributed.

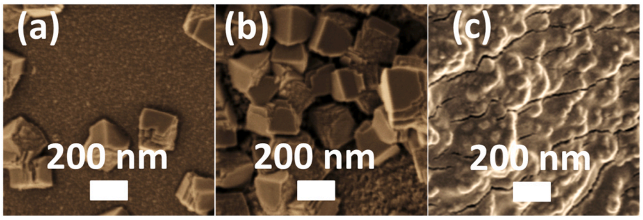

Fig. 1. SEM images of (a) MnCr-MOF-10 min, (b) MnCr-MOF-20 min and (c) MnCr-MOF-30 min.

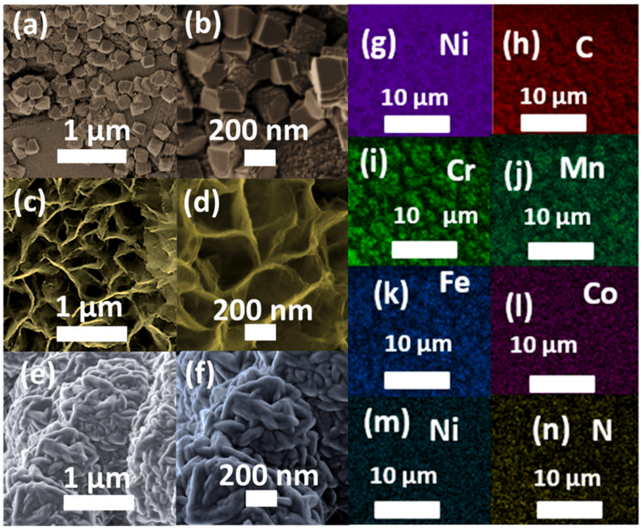

Fig. 2. **(a, b), (c, d)** and **(e, f)** present low- and high-resolution micrographs of MnCr-MOF-20 min, CoNiFe-LDH and MOF-20 min@ CoNiFe-LDH, respectively. **(g–n)** EDS mapping of MOF-20 min@ CoNiFe-LDH.

In Fig. 3(a) for MnCr-MOF-20 min, the oxygen (14.8 ± 0.1 %) comes from the metal-oxygen coordination, the high proportion suggest an oxygen rich porous MOF while, Mn (4.9 ± 0.1 %) and Cr (4.2 ± 0.1 %) are part of the metal nodes, the high proportion of nickel due to the nickel substrate show that the deposited MOF film is thin. In Fig. 3(b) for CoNiFe-LDH, Co (0.8 ± 0.1 %), Ni (98.5 ± 0.1 %), and Fe (0.6 ± 0.1 %) are from the metal centres while the high proportion of the nickel is due to the Ni substrate. In Fig. 3(c) for MOF-20 min@ CoNiFe-LDH, all the elements from MnCr-MOF-20 min and CoNiFe-LDH are present, the drop in the Ni proportion to 75.8 % suggest better coverage of the substrate.

Fig. 4 shows the TEM image MOF-20 min @ CoNiFe-LDH. The MOF nanostructures show a dense array surrounded by sheets of LDH nanosheets. This arrangement is related to the amalgamated SEM image in

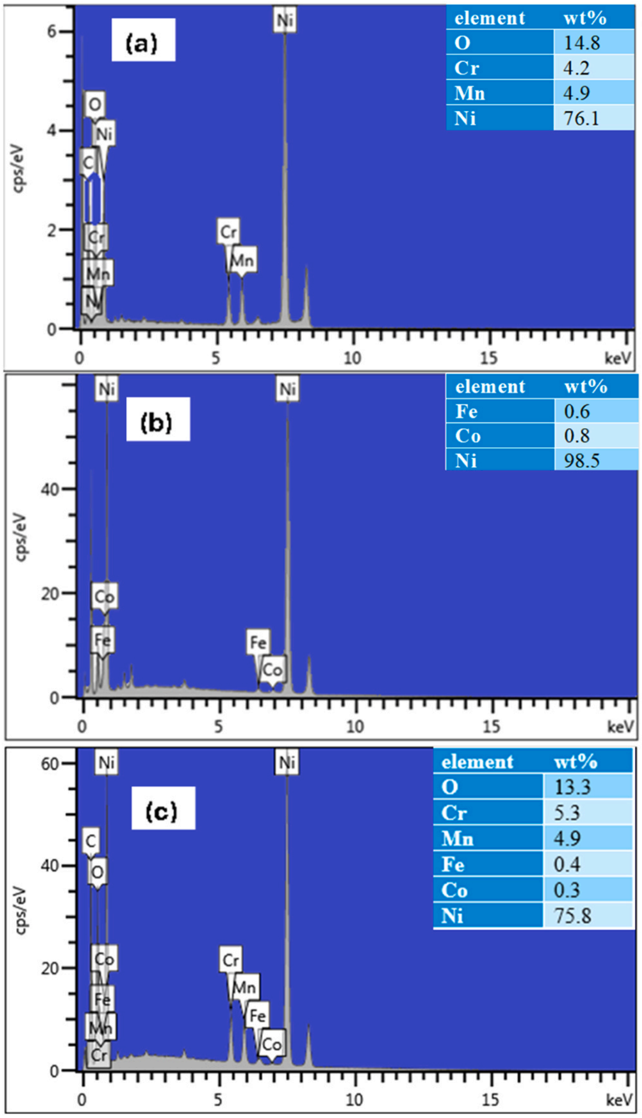

Fig. 3. EDS spectra of (a) MnCr-MOF-20 min, (b) CoNiFe-LDH and (c) MOF-20 min@ CoNiFe-LDH. The inserts show the proportions of the elements.

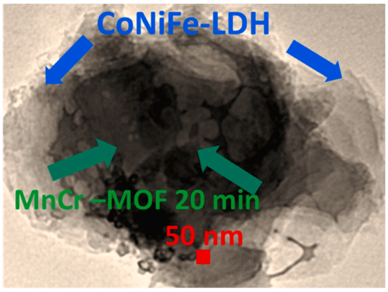

Fig. 4. TEM image of MOF-20 min@ CoNiFe-LDH.

Fig. 2(f).

Fig. 5(a) shows the Raman spectrum of MnCr-MOF-20 min, CoNiFe-LDH and MOF-20 min @ CoNiFe-LDH in the Raman shift range of 100–3000 cm^{-1}. 463 ± 1 cm^{-1} is the bending of the metal-nitrogen or metal-oxygen bond. 643 ± 1 cm^{-1} corresponds to the stretching of the meatal nitrogen bond and the C-N out-of-plane bending of the aromatic ring contributes to the peak at 855 ± 1 cm^{-1}. The stretch of the C-N bond and the N-H wag are responsible for the 1428 cm^{-1} peak. The stretching of the C═N and C═C bond causes the 1674 ± 1 cm^{-1} vibrational mode. Finally, the peak at 2926 ± 1 cm^{-1} is due to the C-H asymmetric stretch in the methyl group [34]. For CoNiFe-LDH, the bending of the metal oxygen bond and the metal hydroxide bond cause the peaks at 504 ± 1 and 545 ± 1 cm^{-1}, respectively. In MOF-20 min @ CoNiFe-LDH, the main peaks for the MOF and the LDH are present, signifying the successful synthesis of the composite [35,36]. The MOF peaks shifted to right in the composite (blue-shift), this can be attributed to the increased crystallinity as the MOF can undergo reorganisation in composite formation causing a blue shift due to diminished vibrational freedom [37].

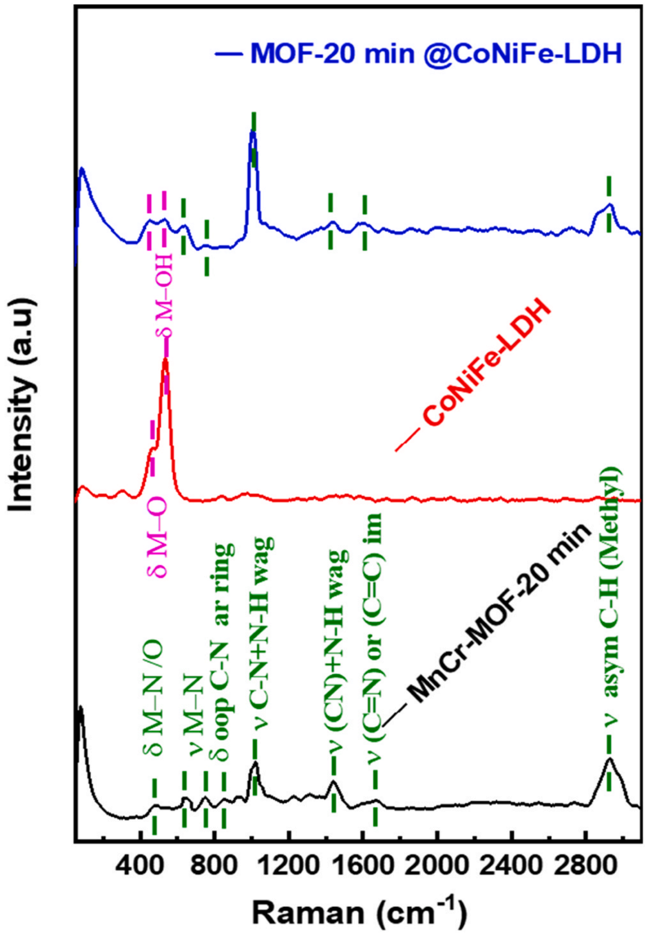

Fig. 5. The Raman spectra of MnCr-MOF-20 min, CoNiFe-LDH and MOF-20 min @ CoNiFe-LDH.

3.2. *Electrochemical performance of the as-synthesized electrode*

3.2.1. *Three-electrode evaluations*

Fig. 6 shows the electrochemical of MnCr-MOF-20 min, CoNiFe-LDH and MOF-20 min @ CoNiFe-LDH in a 3-electrode set-up using 3 M KOH as an electrolyte. Fig. 6(a) shows the CV curves of these electrodes in a potential difference range of 0–0.4 V vs Ag/AgCl. All the curves are characterised by peaks this shows that the Faradaic redox reaction is the most dominant energy storage in all the electrodes. The composite electrode, MOF-20 min @ CoNiFe-LDH shows the largest current response and the most prominent peak, this can be credited to the presence of the additional LDH metal sites into the frameworks which enhances redox reaction while the electrical conductivity is improved by the formation of oxygen vacancies [38]. The peak of the composite is shifted to the right meaning more electrical energy is required for oxidation to occur, this is due to the metal centres (Co, Ni and Fe)

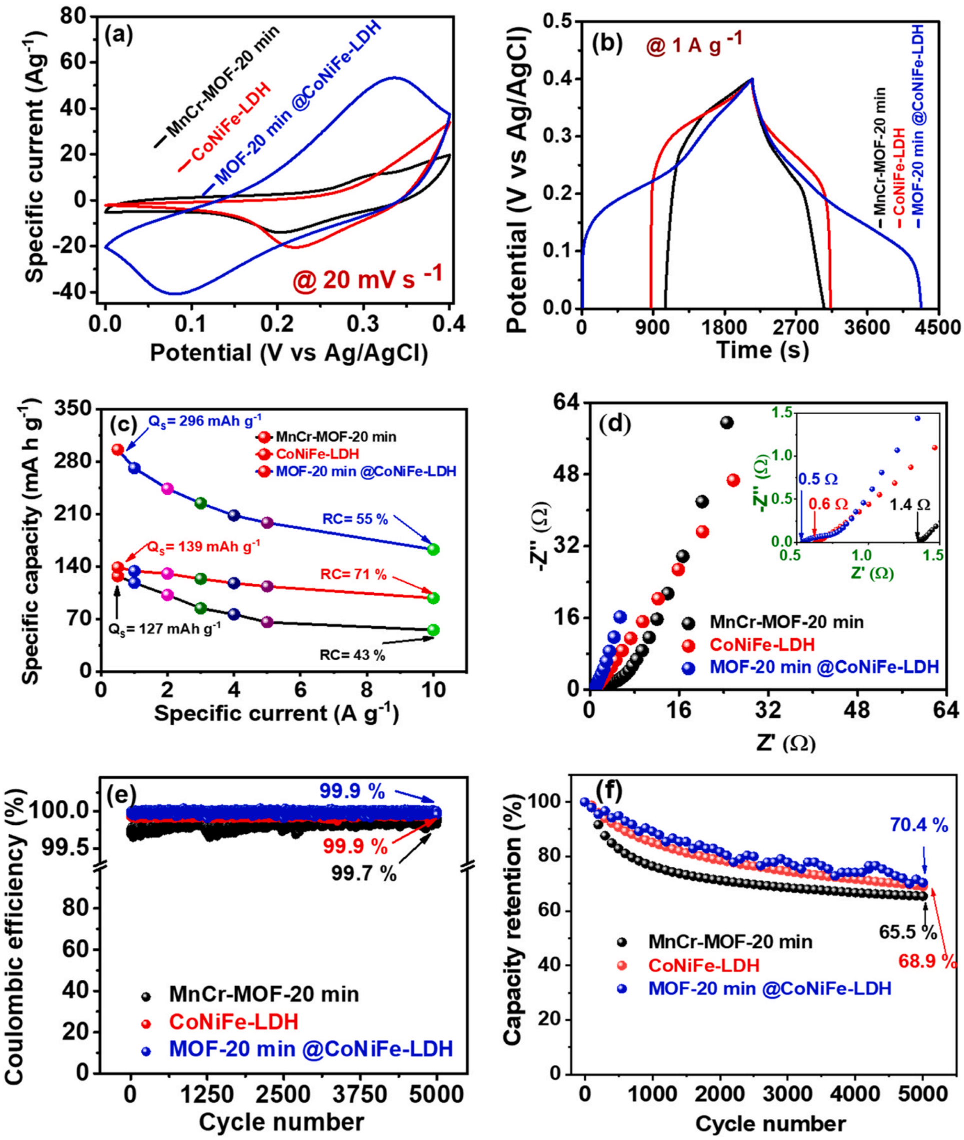

Fig. 6. Electrochemical comparison of MnCr-MOF-20 min, CoNiFe-LDH and MOF-20 min @ CoNiFe-LDH; (a) CV curves, (b) GCD curves, (c) specific capacity vs specific current, (d) EIS Nyquist plot (the inset is magnified high frequency region), (e) Coulombic efficiency and (f) capacity retention.

experiencing stronger coordination with the MOF. Fig. 6(b) shows the GCD curves of the three electrodes, the inclined plateaus are a further testimony of the redox reactions [39]. The most prolonged discharge time of MOF-20 min @ CoNiFe-LDH echoes the current response shown in Fig. 6(a). Fig. 6(c) shows the plots of specific capacity as a function of specific current. The specific capacity (Q_s) was calculated using Eq. 1 [40]:

$$Q_s \quad \left[\text{mAhg}^{-1}\right] = \frac{1}{3.6} I_s \Delta t \tag{1}$$

where I_s is the specific current $\left(\text{Ag}^{-1}\right)$ and Δt is the discharge time (s). The specific capacities at the specific current of 1 A g^{-1} are 127, 139 and 296 ± 5 mAh g^{-1} for MnCr-MOF-20 min, CoNiFe-LDH and MOF-20 min @ CoNiFe-LDH, respectively. The superior specific capacity of MOF-20 min @ CoNiFe-LDH shows the benefit of combining the LDH and MOF to take advantage of the individual attributes of the individual electrodes. Fig. 6(d) is the EIS Nyquist plot of the three electrodes for a frequency range of 10 mHz to 100 kHz. The complex impedance and its magnitude are in terms of its real and imaginary impedance as shown in Eqs. (2) and (3):

$$Z(\omega) = Z'(\omega) + jZ''(\omega) \tag{2}$$

$$|Z(\omega)|^2 = Z'(\omega)^2 + Z''(\omega)^2 \tag{3}$$

Where $Z(\omega)$, $|Z(\omega)|$, $Z'(\omega)$ and $Z''(\omega)$ are the complex impedances, the magnitude of the complex impedance, the real and imaginary impedance (Ω), repectively, $\omega = 2\pi f$ is the angular frequency (rad s^{-1}) and $j = \sqrt{-1}$, is the imaginary number.

The equivalent series resistance (ESR) values are 1.4, 0.6 and 0.5Ω for MnCr-MOF-20 min, CoNiFe-LDH and MOF-20 min @ CoNiFe-LDH, respectively. The values show that combined resistance at the electrode-current collector and the electrode-electrolyte are all low, this can be attributed to the electrodeposition synthesis route which ensures a strong adhesion of the electrode material to the current collector which also improves the electronic conductivity [27,41,42]. Furthermore, MOF-20 min @ CoNiFe-LDH has the lowest ESR value and the shortest diffusion length of the plot along the imaginary impedance $(Z''(\omega))$ axis, this signifies a higher specific capacitance since capacitance is inversely proportional to imaginary impedance [43]. Fig. 6(e) shows a comparison of the coulombic efficiency of samples for 5000 GCD cycles at

12 A g^{-1}.

The coulombic efficiency (η) was calculated using Eq. (4) [44,45]:

$$\eta[\%] = \frac{\Delta t_D}{\Delta t_C} \times 100 \quad \% \tag{4}$$

where Δt_C and Δt_D are charging and discharging times (s) respectively. The coulombic efficiency values are 99.7, 99.9 and 99.8 ± 0.1 % for MnCr-MOF-20 min, CoNiFe-LDH and MOF-20 min @ CoNiFe-LDH, respectively. The capacity retention of the electrodes was plotted in Fig. 6(f). The capacity retention at the 5000th cycle was, 65.5, 68.9 and 70.4 ± 0.1 % for MnCr-MOF-20 min, CoNiFe-LDH and MOF-20 min @ CoNiFe-LDH, respectively. These extremely high stability values show near-perfect reversibility of the redox reaction while performing GCD [46].

These results show that the electrochemical performance of MOF-20 min @ CoNiFe-LDH surpasses that of MnCr-MOF-20 min and CoNiFe-LDH, which could be due to the composite electrode benefiting from the synergetic effect of the individual electrode materials with the MOF availing large surface area with adjustable pore sizes and the LDH contributing to the increase in the rate capability and electrical conductivity. For this reason, MOF-20 min @ CoNiFe-LDH was chosen for further analysis.

Fig. 7 shows the electrochemical analysis of MOF-20 min @ CoNiFe-LDH in 2 M KOH, in a three-electrode configuration. Fig. 7(a) shows the CV plot in a potential difference range of 0.0–0.4 (V vs Ag/AgCl). The plots show redox peaks which diminish as the scan increases. This is the effect of the diffusion of electrolyte ions into the electrode material pores, and this occurs more efficiently at low scan rates. This is due to the limited interaction time between electrode active species and the electrolyte ions as the scan rate increases, the broadening of the peaks is due to electrode resistance [47,48]. The shift of the reduction and oxidation peaks towards higher potentials is caused by a build-up in resistance as scan rate increase signifying a drop in reversibility[49]. The prevailing energy storage mechanisms taking place can best be evaluated by expressing the specific current (I_s) from the CV as a function of the scan rate (ν) using the power law shown in Eq. (5) [50]:

$$I_S(V) = a\nu^b \tag{5}$$

where a and b are constants which can be obtained after linearization as shown in Eq. (6):

$$\log I_s(V) = a + b\log\nu \tag{6}$$

After plotting a linear graph of $\log I_s$ (V) vs $\log\nu$, a and b will be the

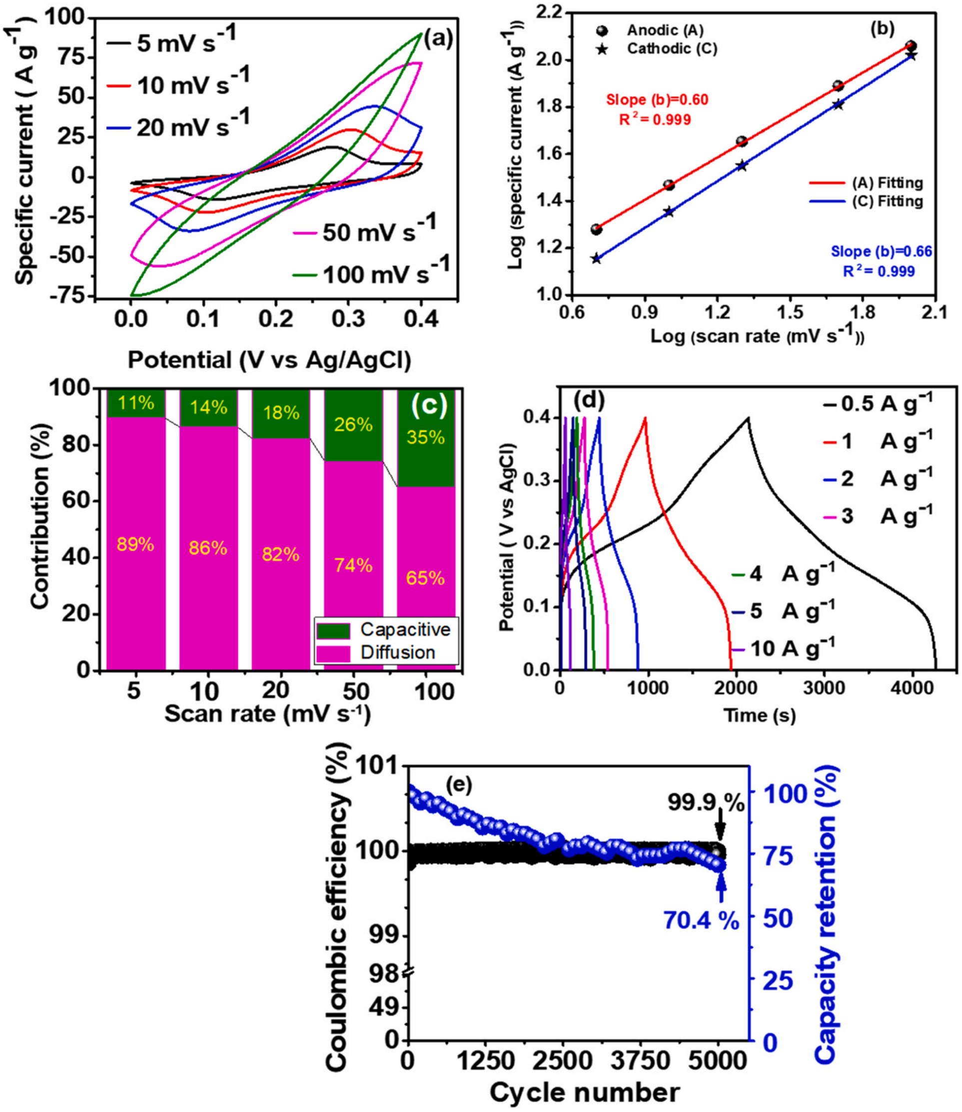

Fig. 7. (a) CV curves, (b) the relationship of log current versus log scan rate (power law - cathodic and anodic), (c) contribution (%) of diffusion-controlled and capacitive charge storage, (d) GCD curves, (e) capacity retention and Coulombic efficiency as a function of cycle number for MOF-20 min @ CoNiFe-LDH.

y-intercept and the gradient. The values of b are in the range of $0.5 \leq b \leq 1.0$, with values approaching 0.5 being for the diffusion-controlled mechanism and 1.0 for the surface-controlled mechanism [51]. Fig. 7(b) shows such a plot; the plot is highly linear as the coefficient of determination, R^2 value of 0.999 ± 0.005 is close to unity. The values of b are 0.60 and 0.66 ± 0.01 for the anodic and cathodic reactions, respectively, these values show that both processes are participating but the diffusion-controlled process dominate the energy storage mechanism of MOF-20 min @ CoNiFe-LDH since the values are closer to 0.5 than to 1.0. For an in-depth analysis of the surface and diffusion-controlled process for a range of scan rates, a model is used which assumes that the current (I(V) partially varies with the scan rate and the square-root of the scan as given by a version of the Dunn model Eq. (7) [52,53]:

$$\mathrm{I(V)} = \mathrm{H}_1\nu + \sqrt{\mathrm{H}_2\nu} \tag{7}$$

Where $\mathrm{H}_1\nu$ and $\mathrm{H}_2\nu$ are the proportions of the specific current contributed by the surface and diffusion-controlled processes, respectively. H_1(F) and H_2 (AF or CS) are the constants obtained by rearranging Eq. (5) and plotting $\frac{\mathrm{I(V)}}{\sqrt{\nu}}$ vs $\sqrt{\nu}$. The values of H_1 and H_2 are the gradient and the square of the y-intercept, respectively. When these values were substituted back into Eq. (5), the surface and diffusion-controlled contribution were calculated and displayed in the bar chart graph in Fig. 7(c). Diffusion-controlled processes dominate all the scan rates while the surface-controlled process increases gradually with the scan rate to reach a maximum of 35 % at a scan rate of 100 mV s^{-1}. Fig. 7(d) shows the GCD for a range of I_s from 1 to 10 A g^{-1}. All the traces show symmetric curves with tilted plateaux, showing high reversible Faradaic reactions characterising the energy storage mechanism of the composite electrode [54]. Fig. 7(e) shows the coulombic efficiency and capacity retention of the electrode for 5000 GCD cycles. The Coulombic efficiency (CE $_\mathrm{N}$) and the ($\mathrm{CR_N}$) of the $\mathrm{N^{th}}$ cycle were calculated using Eqs. (8) and (9):

$$\varepsilon[\%] = \frac{\Delta t_{DN}}{\Delta t_{CN}} \tag{8}$$

$$CR_N[\%] = \frac{\Delta t_{DN}}{\Delta t_{D1}} \tag{9}$$

Where Δt_{DN} and Δt_{CN} are the discharging and charging times (s) for the $\mathrm{N^{th}}$ cycle respectively and Δt_{D1} and Δt_{DN} are the discharge times (s) for the first and $\mathrm{N^{th}}$ cycle, respectively. The coulombic efficiency and the capacity retention were 99.8 ± 0.1 % and 87.0 ± 0.1 %, respectively after 5, 000 cycles. This shows great electrochemical stability which can be credited to the electrodeposition method which ensures robust bonding of the electrode material to the current-collector and the synergetic effect of the LDH and the MOF.A comparison of the MOF-20 min @ CoNiFe-LDH with some bimetallic MOFs composite electrodes reported in literature is summarised in Table 1. The specific capacity for this electrode is significantly higher than those of some electrode reported in literature as shown in the table. The capacity retention is comparable with some of the electrodes. This makes the electrode suitable for incorporation into a supercapacitor device.

3.2.2. *Electrochemical performance of the supercapacitor device*

To evaluate its performance when integrated into a supercapacitor device, MOF-20 min @ CoNiFe-LDH was incorporated in a coin-cell asymmetric supercapacitor MOF-20 min @ CoNiFe-LDH//AMH device as a positive electrode while activated carbon from Amarula husk (AMH) served as the negative electrode in 2 M KOH electrolyte. Mass balance was employed to ensure that electrodes do not end up charging each other, this was done according to Eq. (10)

$$\frac{\mathrm{m}_-}{\mathrm{m}_+} = \frac{3.6 \quad \mathrm{Q}_{S+}}{\mathrm{C}_-\mathrm{V}_-} \tag{10}$$

Where $\mathrm{m}\_/\mathrm{m}_+$ is the mass ratio of the negative to the positive electrode materials, Q_{S+} is the specific capacity of the positive electrode while $C\_$ and V_- are the specific capacitance (Fg^{-1}) of the electrode and the electrode potential (V) respectively, of the negative electrode. The calculated mass ratio m_- : m_+ was approximately 6:1 hence the mass loading on the negative and positive mass ratios were 6.0 mg ± 0.1 cm^{-2} and 1.0 ± 0.1 mg cm^{-2}, respectively. This gives electrode mass of 7.0 mg ± 0.2 cm^{-2} for the coin cell device.

Fig. 8(a) shows the CV curves of the MOF-20 min @ CoNiFe-LDH and AMH at a scan rate of 20 mV s^{-1}. The trace of AMH lacks peaks due to electric double-layer capacitance (EDLC) which is a characteristic of carbon materials like activated carbon, this is in contract with the curve of MOF-20 min @ CoNiFe-LDH which shows prominent Faradaic peaks. Fig. 8(b) to (f) shows the electrochemical performance of MOF-20 min @ CoNiFe-LDH//AMH. The CV in Fig. 8(b) shows EDLC tendencies at lower potentials while the higher potential windows resemble to the Faradaic charge storage mechanism with the high current response. The device is able to reach a potential of 1.5 V even though the individual negative and positive reached −0.8 V and 0.4 V vs Ag/AgCl in the half-cell set-up respectively, this is because in the 3-electrode set-up, the potential difference is measured between the WE and the RE and the −0.8 V and 0.4 V may not be the maximum voltage that is attainable by then negative and positive electrodes respectively. However, in the device, the potential in a 2-electrode set-up are between the negative and positive electrodes and careful mass balance can enable the individual electrodes to achieve their maximum potential [61]. The maximum of 1.5 V for our asymmetric device instead of just 1.2 V cell potential due to the careful mass balancing for the asymmetric device. An activated carbon and a MOF based electrode can separately reach −1.0 and 0.5 V vs Ag/Ag respectively in aqueous electrolyte. This makes it possible to attain a maximum cell voltage of 1.5 V in a device since cell voltage will be $\Delta\mathrm{V} = \mathrm{V}_1 - (\text{-}\mathrm{V}_2)$ and can even reach much higher than this due to the mass balancing in a case of asymmetric device, which is the case for our asymmetric device.[62,63]. Fig. 8(c) shows the GCD at a range of specific currents from 1 to 10 A g^{-1}. The curves possess no visible plateaux, yet they are semi-linear, this shows the existence of both Faradaic and EDLC charge storage mechanisms in the asymmetric device which can be characterized as pseudocapacitive. From the GCD, the specific

Table 1
Electrochemical performance of recently reported bimetallic MOF composites in three-electrode systems.

Material	Synthesis method	Capacity (mAh g^{-1})	Capacity retention/ (cycles)	Ref.
$\mathrm{NiCo_2O_4/\beta\text{-}Ni_xCo_{1\text{-}x}(OH)_2}$ $\mathrm{/\alpha\text{-}Ni_xCo_{1\text{-}x}(OH)_2}$	Hydrolysis and selective oxidation	164 (5 A g^{-1})	90.7 % (10000)	[55]
Ni/Co-MOF	Hydrothermal	158 (1 A g^{-1})	75.5 % (3000)	[56]
Ni–Fe–O/NPC	Calcination	197 (1 A g^{-1})	88.5 % (10000)	[57]
(Ni-Fe)-P-C@HCNFs	Electrospinning and carbonization	193 (1 Ag^{-1})	89 % (10000)	[58]
CuCe-MOF@PANI−1	Hydrothermal and electrodeposition	193 (1 Ag^{-1})	90 % (10000)	[59]
NiCo MOF/VGN	Solvothermal	132 (1 A g^{-1})	92.3 % (10000)	[60]
MOF−20 min @ CoNiFe-LDH	**Electrodeposition**	**296 (0.5 A g^{-1})**	**70.4 ±0.1 % (5000)**	**This work**

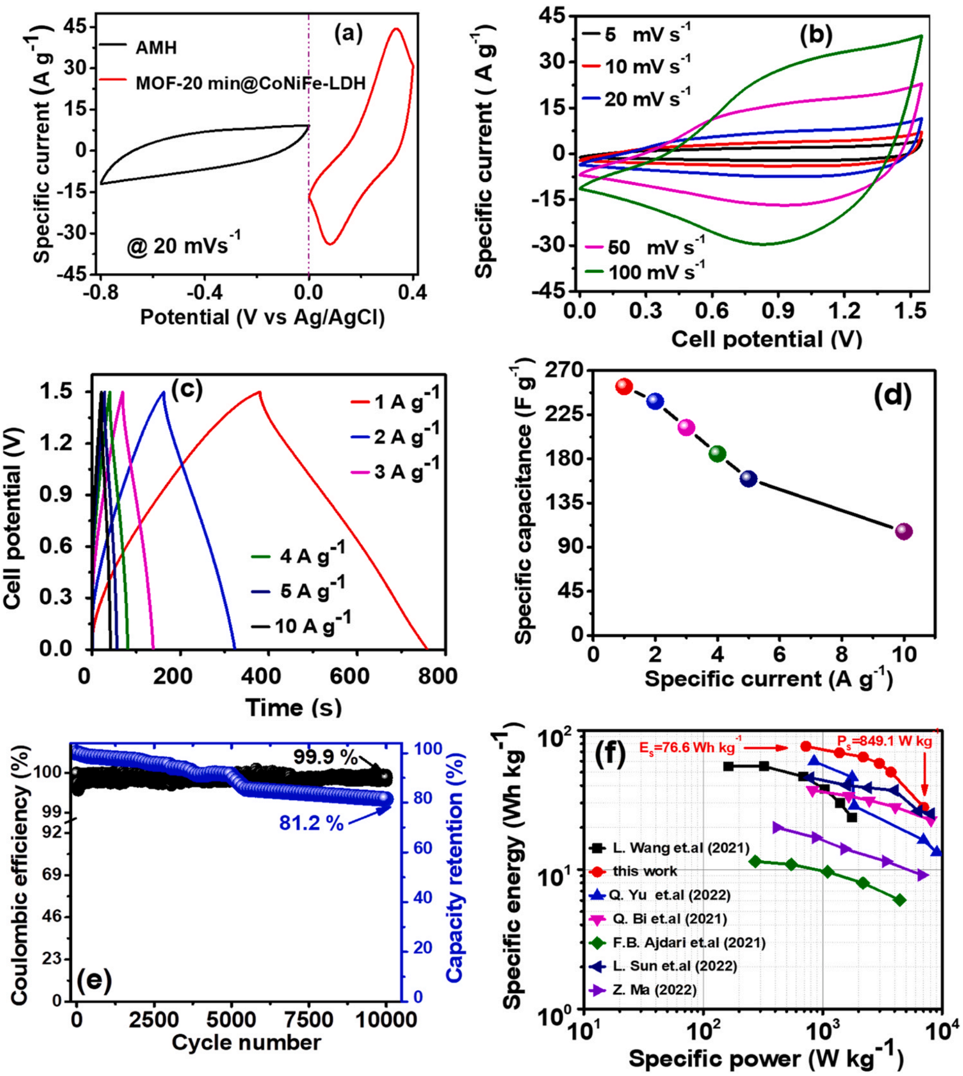

Fig. 8. (a) CV curves of (AMH), (MOF-20 min @ CoNiFe-LDH) at 20 mV s^{-1}, b) CV curves at different scan rates, (c) GCD traces at different specific currents, (d) the specific capacitance vs specific current, (e) capacitance retention and coulombic efficiency vs cycle number and (f) Ragone plot of MOF-20 min @ CoNiFe-LDH// AMH compared to similar devices in the literature.

capacitances were plotted for the range of specific current as shown in Fig. 8. (d). The specific capacitance is calculated from the GCD using Eq. (11).

$$C\left[Fg^{-1}\right] = \frac{I_S \Delta t_D}{V} \tag{11}$$

The rate capability of at 10 A g^{-1} is 48 ± 1 % which is less than that of MOF-20 min @ CoNiFe-LDH is due to the increased thickness of the negative electrode causing extended diffusion routes and diminished porosity[64]. The high thickness was prompted by the need to attain the high mass balance ratio in the device $m\_/m_{+}$.

The highest specific capacitance of 254 F g^{-1} was obtained at a specific current of 1 A g^{-1}. GCD stability at a specific current of 10 A g^{-1} was performed to determine the stability of the device. The coulombic efficiency and the capacity retention only dropped to 99.9 and 81.2 ± 0.1 % after 10, 000 GCD cycles, respectively.

This high stability is caused by the synergetic effect of the carbon electrode material and metal oxide. The specific energy (E_S) and specific power (P_S) for the given range of specific currents were calculated using the area under the GCD in Fig. 8(c) using Eqs. (12) and (13):

$$E_s \quad \left[Wh\ kg^{-1}\right] = \frac{I_s}{3.6}\int_0^V V(t)dt \tag{12}$$

$$P_s \quad \left[W \quad kg^{-1}\right] = 3600 \times \frac{E_s}{\Delta t_D} \tag{13}$$

where I_S represents the specific current (A g^{-1}), the integral $\int_0^V V(t)dt$ is an area under the GCD (Vs) during discharge and Δt_D is the discharge time (s). The highest specific energy of the device was 76.6 ± 0.1 Wh kg^{-1} with corresponding specific power of 724.9 ± 0.1 W kg^{-1} at a specific current of 1 A g^{-1}.

To make a comparison of the power and energy performance of the MOF-20 min @ CoNiFe-LDH//AMH device (this work) with other related devices in literature which incorporate MOF and LDH composites electrodes, the Ragone plot Fig. 8. (f) was constructed [65–70]. The specific energy and specific power obtained compares favourably with the other related devices in the literature if not more.

Fig. 9(a) shows the Nyquist plot of EIS experiment data of the device MOF-20 min @ CoNiFe-LDH//AMH, the inset shows the equivalent circuit used for fitting the data. Fig. 9(b) shows the Nyquist plot of the device before and after 10 000 GCD cycles. The intercept of the curve with the real impedance axis at the high-frequency region is represented on the circuit as R_S corresponding to ESR. It is observed from the table

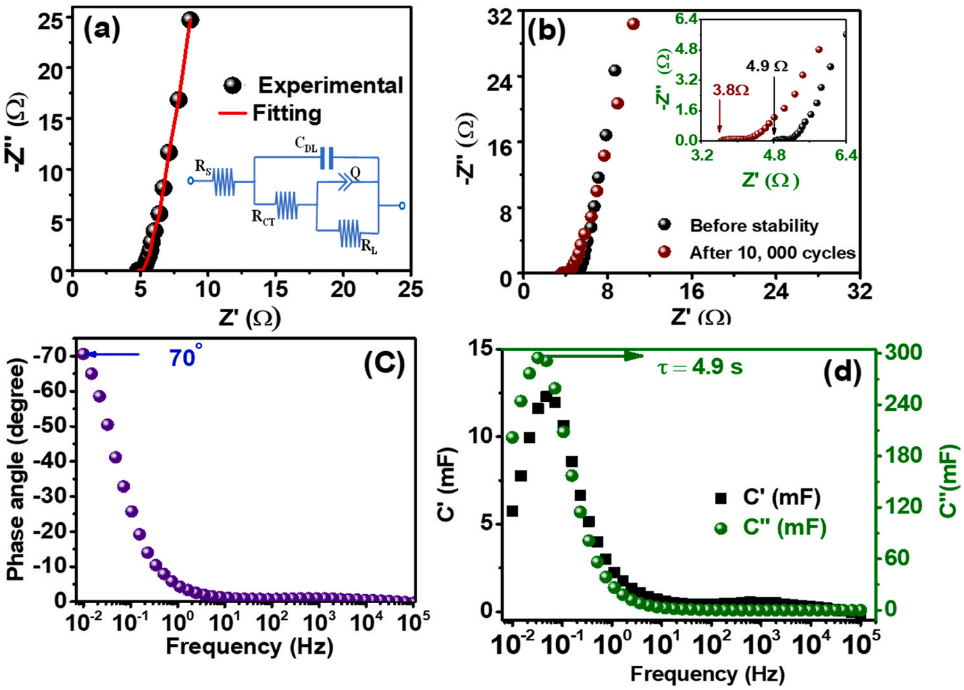

Fig. 9. (a) Nyquist plot for the experimental data with the fitting curve using the equivalent circuit as the inset, (b) Nyquist plot before and after 10, 000 GCD cycles the inset is the enlargement of the higher frequency region, (c) the Bode plot and (d) Real and imaginary capacitance vs frequency of the device.

that R_S drops from 4.9 to 3.8 Ω after cycling proving that MOF-20 min @ CoNiFe-LDH//AMH has high electric conductivity and good stability [71].

This R_S is in series with a branch which contains R_{CT}, the charge transfer resistance, which is the impedance caused by Faradaic reactions [72,73], and correspond to diameter of the semicircle on the experimental curve [74]. R_{CT} increases slightly from 0.3 to 0.4 Ω after GCD stability test. This slight increase can be attributed to the distortions of the pathways due to ion movement during cycling. This also leads to the curve at the lower frequency region getting less steep after cycling and this is caused by the ion diffusion getting less rapid resulting in the drop of C_{DL} from 2.0 to 1.3 ± 0.1 mF. C_{DL} in the parallel branch is the double-layer capacitor which manifests in the low-frequency regime, this is responsible for the curve aligning towards the imaginary impedance. These EDLC tendencies emanate from the AMH in the device. The semicircle is depressed due to the existence of the constant phase element (CPE) represented in the circuit as R_{CT} [75]. CPE is due to the imperfections in the supercapacitor which can be caused by charged impurities in the substrate and/or defects in the electrode material [76]. The CPE impedance is given by Eq. (14) [77]:

$$Z_{CPE}[\Omega] = \frac{1}{Q_0(j\omega)^{\alpha}} \tag{14}$$

Where α is the dimensionless exponent $(0 \leq \alpha \leq 1)$. When $\alpha = 0$, the element is a conductor and when $\alpha = 1$, it is a capacitor. Q_0 is modelled by a circuit element which on one extreme is a capacitor and on the other extreme it is an electrical conductor $(Fs^{\alpha-1})$. The value of α reduces slightly from 0.9 to 0.8 after cycling. It remains close to unity denoting the close resemblance of the CPE to capacitor rather than a conductor/resistor. The Q_0 value changes from $0.5\ F\ s^{-0.1}$ to $0.3\ F\ s^{-0.2}$. This pseudocapacitance drop is due to the diffusion becoming less rapid. R_L in parallel with the CPE is the impedance due to the leakage currents or self-discharge. The increase of R_L form 5.3–12.1 ± 0.1 GΩ is due to the increase in the movement and redistribution of charge carriers as they penetrate the depth of the pores, due to cycling [78].

The parameters for the fitting of the Nyquist plot of the MOF-20 min @ CoNiFe-LDH//AMH before and after cycling for 10, 000 cycles are shown in Table 2.

Fig. 9(c) displays the Bode plot to show the variation of the phase angle with the frequency. The phase angle obtained at 10 mHz is −70°, which is closer to -90^0 which is the ideal value for a capacitive device. Fig. 9(d) shows the plot of the variation of the real $(C'(\omega))$ and imaginary capacitance $(C''(\omega))$ with frequency.

The complex capacitance C(ω) is expressed as the complex impedance as shown in Eq. (15):

$$Z(\omega)[\Omega] = \frac{1}{j\omega C(\omega)} \tag{15}$$

After rearranging, Eq. (16) is obtained:

$$C(\omega)[F] = \frac{1}{j\omega(Z'(\omega) + jZ''(\omega))} = -\frac{Z''(\omega))}{\omega|Z(\omega)|^2} - j\frac{(Z'(\omega))}{\omega|Z(\omega)|^2} \tag{16}$$

The complex capacitance can be resolved into the real and imaginary capacitance components as shown in Eq. 17:

$$C(\omega) = C'(\omega) - jC''(\omega) \tag{17}$$

Where the real and imaginary capacitance are shown in Eqs. (18) and (19):

$$C'(\omega)[F] = -\frac{Z''(\omega)}{|Z(\omega)|^2} \tag{18}$$

Table 2
Nyquist plot fitting parameters before and after 10, 000 GCD cycles of MOF-20 min @ CoNiFe-LDH//AMH.

Parameter	Before 10, 000 GCD cycles	After 10, 000 GCD cycles
R_S	4.9 ± 0.1 Ω	3.8 ± 0.1 Ω
C_{DL}	2.0 ± 0.1 mF	1.3 ± 0.1 mF
R_{CT}	0.3 ± 0.1 Ω	0.4 ± 0.1 Ω
Q	0.5 ± 0.1 $F^{\alpha-1}$	0.3 ± 0.1 F $s^{\alpha-1}$
α	0.9 ± 0.1	0.8 ± 0.1
R_L	5.3 ± 0.1 G Ω	12.1 ± 0.1 G Ω

$$C^{\prime\prime}(\omega)[\mathrm{F}] \quad = \frac{Z^{\prime}(\omega)}{|Z(\omega)|^{2}} \tag{19}$$

where $\omega = 2\pi f$ is the angular frequency (rad s^{-1}). $C^{\prime}(\omega)$ is the accessible capacitance of the cell that is deliverable, it decreases with frequency since the penetration of the ions into the pores is impeded at elevated frequencies, where it approaches zero and the capacitor behaves like a resistor. $C^{\prime\prime}(\omega)$ corresponds to energy lost through irreversible processes such as the rotation of the electrolyte ions. Its peak value occurs at the characteristic frequency (f_0), where the transformation from resistive to capacitive behaviour of the capacitor is considered to occur. This leads to the determination of the relaxation time, $\tau = \frac{1}{\omega}$. This is the minimum time (s) taken to deliver the stored energy with an efficiency which exceeds half of its maximum value. The obtained value of 4.9 ± 0.1 s is small, and this denotes the good charge-discharge rate performance of the device. At f_0, the resistive and capacitive reactance are balanced. [79–82].

4. Conclusion

MnCr-MOF was electrodeposited on NF using chronopotentiometry electrodeposition. The electrode was labelled MOF-20 min, with an electrodeposition time of 20 min. The same procedure was used to electrodeposit CoNiFe-LDH on MnCr-MOF-20 min. The successful synthesis of an LDH and MOF composite was verified through morphological and structural characterisation. The electrode yielded a high specific capacity of 296 ± 5 mAh g^{-1} at a specific current of 0.5 A g^{-1}. The composite electrode, MOF-20 min @ CoNiFe-LDH was then set as the positive electrode in the asymmetric device MOF-20 min @ CoNiFe-LDH//AMH. The device yielded a remarkable specific energy of 76.6 ± 0.1 Wh kg^{-1} at a specific power of 724.9 ± 0.1 W kg^{-1}. Stability measurements of the device resulted in a high capacitance retention of 81.2 ± 0.1 % at 10, 000 cycles at 10 A g^{-1}. With this high electrochemical performance, the device can contribute to energy storage applications successfully.

CRediT authorship contribution statement

Ncholu Manyala: Writing – review & editing, Visualization, Supervision, Resources, Funding acquisition, Formal analysis. **Hellen Ngunya Mutua:** Writing – review & editing, Writing – original draft, Methodology, Conceptualization. **Kabir Opeyemi Otun:** Writing – review & editing, Writing – original draft, Methodology, Formal analysis. **Vianney Ngoyi Kitenge:** Writing – review & editing, Writing – original draft, Methodology, Formal analysis. **Vusani Muswa Maphiri:** Writing – review & editing, Writing – original draft, Methodology, Formal analysis, Conceptualization. **Delvina Japhet Tarimo:** Writing – review & editing, Writing – original draft, Methodology, Formal analysis. **RUTAVI GIFT:** Writing – review & editing, Writing – original draft, Methodology, Investigation, Formal analysis, Data curation.

Declaration of Generative AI and AI-assisted technologies in the writing process

During the preparation of this work the authors used Grammarly to help correct grammar. After using this service, the authors reviewed and edited the content as needed and took full responsibility for the content of the published article.

Declaration of Competing Interest

The authors declare that they have no known competing financial interests or personal relationships that could have appeared to influence the work reported in this paper

Acknowledgements

This research was enabled by the Bilateral project between NRF, South African and Italy (ISARP) (Grant number 2204072535). All the ideas, findings, recommendations, and conclusions in this work are of the author(s) hence NRF does not take any liability in this regard. Gift Rutavi recognises the support from NRF ISARP project.

Data availability statement

Data will be made available on request.

References

[1] H. Bhattarai, Renewable energy and energy storage systems, Energy Convers. Methods Technol. Futur. Dir. (2022) 269–289, https://doi.org/10.52305/wxnj6607.

[2] M. Jafari, A. Botterud, A. Sakti, Decarbonizing power systems: a critical review of the role of energy storage, Renew. Sustain. Energy Rev. 158 (2022) 112077, https://doi.org/10.1016/j.rser.2022.112077.

[3] M.A. Rahman, J.H. Kim, S. Hossain, Recent advances of energy storage technologies for grid: a comprehensive review, Energy Storage 4 (2022) 1–28, https://doi.org/10.1002/est2.322.

[4] K. Dhamodharan, A.K. Singh, Synthesis of hybrid SmMnO3/rGO nanocomposites for high performance energy storage applications, J. Alloy. Compd. 976 (2024) 173087, https://doi.org/10.1016/j.jallcom.2023.173087.

[5] A.G. Olabi, Q. Abbas, A. Al Makky, M.A. Abdelkareem, Supercapacitors as next generation energy storage devices: properties and applications, Energy 248 (2022) 123617, https://doi.org/10.1016/j.energy.2022.123617.

[6] M.B.F. Ahsan, S. Mekhilef, T.K. Soon, M.B. Mubin, P. Shrivastava, M. Seyedmahmoudian, Lithium-ion battery and supercapacitor-based hybrid energy storage system for electric vehicle applications: a review, Int. J. Energy Res. 46 (2022) 19826–19854, https://doi.org/10.1002/er.8439.

[7] T. Liang, Z. Mao, L. Li, R. Wang, B. He, Y. Gong, J. Jin, C. Yan, H. Wang, A mechanically flexible necklace-like architecture for achieving fast charging and high capacity in advanced lithium-ion capacitors, Small 18 (2022) 1–12, https://doi.org/10.1002/smll.202201792.

[8] Z. Salehi Rozveh, M. Pooriraj, M. Rad, V. Safarifard, M. Moradi, Synergistic effect of metal node engineering and mixed-linker-architected on the energy storage activities of pillar-layered Cu2(L)2(DABCO) metal-organic frameworks, Mater. Chem. Phys. 292 (2022) 126761, https://doi.org/10.1016/j.matchemphys.2022.126761.

[9] A. Pramitha, Y. Raviprakash, Recent developments and viable approaches for high-performance supercapacitors using transition metal-based electrode materials, J. Energy Storage 49 (2022) 104120, https://doi.org/10.1016/j.est.2022.104120.

[10] X.W. Wang, Q.Q. Zhu, X.E. Wang, H.C. Zhang, J.J. Zhang, L.F. Wang, Structural and electrochemical properties of La0.85Sr0.15MnO3 powder as an electrode material for supercapacitor, J. Alloy. Compd. 675 (2016) 195–200, https://doi.org/10.1016/j.jallcom.2016.03.048.

[11] H. Rong, P. Song, G. Gao, Q. Jiang, X. Chen, L.X. Su, W.L. Liu, Q. Liu, A three-dimensional Mn-based MOF as a high-performance supercapacitor electrode, Dalt. Trans. 52 (2023) 1962–1969, https://doi.org/10.1039/d2dt02857c.

[12] G. Ryoo, S.K. Kim, D.K. Lee, Y. Kim, Energy Storage Performance of Electrode Materials Derived from Manganese Metal – Organic Frameworks, (2024).

[13] M.Z. Iqbal, U. Aziz, S. Siddique, S. Aftab, S.M. Wabaidur, Effect of distinct organic ligands on hierarchical porous manganese-based MOFs for battery-supercapacitor hybrid, Mater. Sci. Semicond. Process 162 (2023) 107511, https://doi.org/10.1016/j.mssp.2023.107511.

[14] H. Zhang, Y. Yang, Y. Deng, B. Guo, X. Jia, G. Zhang, G. Li, K. Wang, Construction of 2D MOF nanosheets with missing-linker defects for enhanced supercapacitor performance, J. Alloy. Compd. 999 (2024) 175049, https://doi.org/10.1016/j.jallcom.2024.175049.

[15] X. Hang, B. Liu, G. Yuan, X. Wang, Y. An, H. Pang, Facile synthesis of 2D bimetallic MOF micro/nanostructures for enhanced supercapacitor, Mater. Today Chem. 34 (2023) 101754, https://doi.org/10.1016/j.mtchem.2023.101754.

[16] M. Adil, A.G. Olabi, M.A. Abdelkareem, H. Alawadhi, A. Bahaa, K. ElSaid, C. Rodriguez, In-situ grown bimetallic FeCu MOF-MXene composite for solid-state asymmetric supercapacitors, J. Energy Storage 68 (2023) 107817, https://doi.org/10.1016/j.est.2023.107817.

[17] K.O. Otun, N.F. Diop, O. Fasakin, R.A.M. Adam, G. Rutavi, N. Manyala, Engineering the structures of ZnCo-MOFs via a ligand effect for enhanced supercapacitor performance, RSC Adv. 15 (2025) 4120–4136, https://doi.org/10.1039/d4ra08192g.

[18] L. Liu, X. Tai, X. Zhou, J. Hou, Z. Zhang, Bimetallic Au–Ni alloy nanoparticles in a metal–organic framework (MIL-101) as efficient heterogeneous catalysts for selective oxidation of benzyl alcohol into benzaldehyde, J. Alloy. Compd. 790 (2019) 326–336, https://doi.org/10.1016/j.jallcom.2019.03.186.

[19] I. Dědek, V. Kupka, P. Jakubec, V. Šedajová, K. Jayaramulu, M. Otyepka, Metal-organic framework/conductive polymer hybrid materials for supercapacitors, Appl. Mater. Today 26 (2022), https://doi.org/10.1016/j.apmt.2022.101387.

[20] S.J. Shin, J.W. Gittins, C.J. Balhatchet, A. Walsh, A.C. Forse, Metal–organic framework supercapacitors: challenges and opportunities, Adv. Funct. Mater. 2308497 (2023) 1–11, https://doi.org/10.1002/adfm.202308497.

[21] F. Ye, J.J. Zhou, X. Jiang, L. Wang, Y. Su, B. Zhu, L. Chen, Hierarchical columnar Cactus-like Co-MOF@NiCo-LDH core-shell nanowrinkled pillar arrays for supercapacitors with ultrahigh areal capacitance, ACS Appl. Energy Mater. 6 (2023) 4844–4853, https://doi.org/10.1021/acsaem.3c00341.

[22] Y. Zhou, X. Song, S. Yan, C. Ni, L. Xu, L. Yu, X. Li, A hierarchical CoNi @ nitrogen doped C/macroporous C composite derived from a new bimetallic MOF and Juncus effusus as a broadband electromagnetic wave absorber, J. Alloy. Compd. 944 (2023), https://doi.org/10.1016/j.jallcom.2023.169146.

[23] G. Rutavi, D.J. Tarimo, V.M. Maphiri, N. Manyala, Two-step electrodeposition of Hausmannite sulphur reduced graphene oxide and cobalt-nickel layered double hydroxide heterostructure for high-performance supercapacitor, Int. J. Energy Res. (2022) 1–14, https://doi.org/10.1002/er.7922.

[24] H. Liu, J. Zhu, Z. Li, Z. Shi, J. Zhu, H. Mei, Fe2O3/N doped rGO anode hybridized with NiCo LDH/Co(OH)2 cathode for battery-like supercapacitor, Chem. Eng. J. 403 (2021) 126325, https://doi.org/10.1016/j.cej.2020.126325.

[25] W. Zheng, S. Sun, Y. Xu, R. Yu, H. Li, Sulfidation of hierarchical NiAl−LDH/Ni−MOF composite for high-performance supercapacitor, ChemElectroChem 6 (2019) 3375–3382, https://doi.org/10.1002/celc.201900687.

[26] P. Forouzandeh, P. Ganguly, R. Dahiya, S.C. Pillai, Supercapacitor electrode fabrication through chemical and physical routes, J. Power Sources 519 (2022) 230744, https://doi.org/10.1016/j.jpowsour.2021.230744.

[27] G. Rutavi, D.J. Tarimo, V.M. Maphiri, V.N. Kitenge, N. Manyala, Assessment of the electrodeposition synthesized manganese chromite and cobalt-nickel layered double hydroxide composite for high-performance supercapacitor applications, J. Energy Storage 58 (2023) 106442, https://doi.org/10.1016/j.est.2022.106442.

[28] X.X. Li, Y.F. Chen, X.M. Zheng, Y.Q. Zhu, Z.W. Wang, Y. Wang, One-step electrodeposition of composition-controllable dendritic NiFe alloy electrocatalysts for oxygen evolution reaction, J. Alloy. Compd. 968 (2023) 172313, https://doi.org/10.1016/j.jallcom.2023.172313.

[29] N.C. Maile, S.K. Shinde, D. –Y. Kim, K.C. Devarayapalli, D.S. Lee, Synthesis of nickel cobalt sulfide on Ni foam for improved electrochemical energy storage: effect of binder-free reverse pulse potentiostatic electrodeposition and redox additive, J. Alloy. Compd. 967 (2023) 171845, https://doi.org/10.1016/j.jallcom.2023.171845.

[30] P. Yao, T. Wang, H. Yu, Z. Li, C. Cheng, J. Zhu, Bi2O3@reduced graphene oxide and NiCo2@Ni3Co electrodes for all-electrodeposited high-performance supercapacitors, J. Power Sources 613 (2024), https://doi.org/10.1016/j.jpowsour.2024.234958.

[31] H. Soltani, H. Bahiraei, S. Ghasemi, Effect of electrodeposition time on the supercapacitive performance of electrodeposited MnO2 on g-C3N4 nanosheets, J. Alloy. Compd. 904 (2022) 163565, https://doi.org/10.1016/j.jallcom.2021.163565.

[32] D.J. Tarimo, A.A. Mirghni, K.O. Oyedotun, G. Rutavi, V.N. Kitenge, N. Manyala, Recycling of biomass wastes from amarula husk by a modified facile economical water salt method for high energy density ultracapacitor application, J. Energy Storage 53 (2022) 105166, https://doi.org/10.1016/j.est.2022.105166.

[33] S. Mao, L. Ye, S. Jin, C. Zhou, J. Pang, W. Xu, Enhanced electrocatalytic oxygen evolution by in situ growth of tetrametallic metal-organic framework electrocatalyst FeCoNiMn-MOF on nickel foam, Inorg. Chem. 63 (2024) 6005–6015, https://doi.org/10.1021/acs.inorgchem.4c00308.

[34] G. Kumari, K. Jayaramulu, T.K. Maji, C. Narayana, Temperature induced structural transformations and gas adsorption in the zeolitic imidazolate framework ZIF-8: a Raman study, J. Phys. Chem. A 117 (2013) 11006–11012, https://doi.org/10.1021/jp407792a.

[35] R.C. Rohit, A.D. Jagadale, S.K. Shinde, D.Y. Kim, V.S. Kumbhar, M. Nakayama, Hierarchical nanosheets of ternary CoNiFe layered double hydroxide for supercapacitors and oxygen evolution reaction, J. Alloy. Compd. 863 (2021), https://doi.org/10.1016/j.jallcom.2020.158081.

[36] P. Wang, S. Song, M. He, C. Li, W. Wang, H. Li, X. Yuan, Z. Fang, K.P. Rinel, W. Song, J. Li, D.G. Vlachos, Z. Li, High-density defects in ordered macroporous-mesoporous CoNiFe-LDHs for efficient and robust oxygen evolution reaction, Chem. Catal. 3 (2023) 100497, https://doi.org/10.1016/j.checat.2022.100497.

[37] Y. Havryliuk, V. Dzhagan, A. Karnaukhov, O. Selyshchev, J. Hann, D.R.T. Zahn, Raman spectroscopy and thermoelectric characterization of composite thin films of Cu2ZnSnS4 nanocrystals embedded in a conductive polymer PEDOT:PSS, Nanomaterials 13 (2023), https://doi.org/10.3390/nano13010041.

[38] X. Luo, R. Abazari, M. Tahir, W.K. Fan, A. Kumar, T. Kalhorizadeh, A.M. Kirillov, A. R. Amani-Ghadim, J. Chen, Y. Zhou, Trimetallic metal–organic frameworks and derived materials for environmental remediation and electrochemical energy storage and conversion, Coord. Chem. Rev. 461 (2022) 214505, https://doi.org/10.1016/j.ccr.2022.214505.

[39] M. Jana, P. Samanta, N.C. Murmu, T. Kuila, Surface modification of reduced graphene oxide through successive ionic layer adsorption and reaction method for redox dominant supercapacitor electrodes, Chem. Eng. J. 330 (2017) 914–925, https://doi.org/10.1016/j.cej.2017.08.046.

[40] G. Rutavi, D.J. Tarimo, V.M. Maphiri, V.N. Kitenge, N. Manyala, Exploration of metal-layered double hydroxide composite material for hybrid capacitor produced by facile and efficient electrodeposition process, J. Alloy. Compd. 929 (2022) 167216, https://doi.org/10.1016/j.jallcom.2022.167216.

[41] P. Shabeeba, M.S. Thayyil, M.P. Pillai, P.P. Soufeena, C.V. Niveditha, Electrochemical investigation of activated carbon electrode supercapacitors, Russ. J. Electrochem. 54 (2018) 302–308, https://doi.org/10.1134/S1023193517120096.

[42] H. Li, S. Sun, W. Cui, X. Li, C. Kou, Z. Xu, Z. Zhang, Fabrication of Co-Fe-Mn composites with a mixed-dimensional structure for applications in high-performance supercapacitors, J. Alloy. Compd. 949 (2023) 169865, https://doi.org/10.1016/j.jallcom.2023.169865.

[43] G. Sharma, C. Dawo, K. Mulchandani, U.K. Kumawat, R.K. Singhal, C. Lal, Revealing the photophysics of N719 dye based dye-sensitized solar cell, Opt. Mater. 142 (2023) 114113, https://doi.org/10.1016/j.optmat.2023.114113.

[44] S. Sarkar, R. Akshaya, S. Ghosh, Nitrogen doped graphene/CuCr2O4 nanocomposites for supercapacitors application: effect of nitrogen doping on coulombic efficiency, Electrochim. Acta 332 (2020) 135368, https://doi.org/10.1016/j.electacta.2019.135368.

[45] A. Joseph, T. Thomas, Synthesis of zirconium oxynitride via ammonia-free soft urea method for an asymmetric supercapacitor with high power density, J. Alloy. Compd. 971 (2024) 172714, https://doi.org/10.1016/j.jallcom.2023.172714.

[46] S. Wu, Y. Yang, M. Sun, T. Zhang, S. Huang, D. Zhang, B. Huang, P. Wang, W. Zhang, Dilute aqueous-aprotic electrolyte towards robust Zn-ion hybrid supercapacitor with high operation voltage and long lifespan, NanoMicro Lett. 16 (2024) 1–12, https://doi.org/10.1007/s40820-024-01372-x.

[47] U. Latif, Z.U. Rehman, M.F. Maqsood, M.A. Raza, S. Ali, M.J. Iqbal, S.M.Z. Mehdi, N. Lee, In situ growth of nickel ammonium phosphate ribbons on nickel foam for supercapacitor applications, J. Energy Storage 73 (2023) 109024, https://doi.org/10.1016/j.est.2023.109024.

[48] B. Jeevanantham, M.K. Shobana, T. Pazhanivel, H. Choe, Pseudocapacitive behaviors of strontium-doped cobalt ferrite nanoparticles for supercapacitor applications, J. Alloy. Compd. 960 (2023) 170651, https://doi.org/10.1016/j.jallcom.2023.170651.

[49] F. Parsapour, M. Pooriraj, M. Moradi, V. Safarifard, S. Hajati, Synthesis of M/Al (M = Co, Ni, Zn) layered double hydroxide derived from aluminum fumarate-based MOF as advanced materials for supercapacitor, Synth. Met. 292 (2023) 117234, https://doi.org/10.1016/j.synthmet.2022.117234.

[50] Q. Xiao, J. Zhu, C. Cheng, J. Liu, X. Zhang, Z. Li, J. Zhu, Battery-like bismuth oxide anodes for soft-packed supercapacitors with high energy storage performance, Nanoscale 15 (2023) 3884–3892, https://doi.org/10.1039/d2nr07096k.

[51] N.T. Bharanitharan, D. Dhinasekaran, M.R. Ashwin Kishore, B. Subramanian, A. R. Rajendran, Rational design of NiCo2O4@carbon hollow spheres as a high-performance electrode material for flexible supercapacitors, Nanoscale (2024) 2252–2258, https://doi.org/10.1039/d4nr04709e.

[52] S.Q. Zheng, S.S. Lim, C.Y. Foo, C.Y. Haw, W.S. Chiu, C.H. Chia, P.S. Khiew, Fabrication of sodium and MoS2 incorporated NiO and carbon nanostructures for advanced supercapacitor application, J. Energy Storage 63 (2023) 106980, https://doi.org/10.1016/j.est.2023.106980.

[53] T. Wang, C. Cheng, Z. Guan, T. Tao, Q. Xiao, J. Zhu, Chemical reduction-induced defect-rich bismuth oxide-reduced graphene oxide anode for high-performance supercapacitors, J. Colloid Interface Sci. 677 (2025) 45–54, https://doi.org/10.1016/j.jcis.2024.07.213.

[54] X. Zhang, M.I. Alvarado-Ávila, Y. Liu, D. Yu, F. Ye, J. Dutta, Self-sacrificial growth of hierarchical P(Ni, Co, Fe) for enhanced asymmetric supercapacitors and oxygen evolution reactions, Electrochim. Acta 438 (2023), https://doi.org/10.1016/j.electacta.2022.141582.

[55] H. Mei, Y. Mei, S. Zhang, Z. Xiao, B. Xu, H. Zhang, L. Fan, Z. Huang, W. Kang, D. Sun, Bimetallic-MOF derived accordion-like ternary composite for high-performance supercapacitors, Inorg. Chem. 57 (2018) 10953–10960, https://doi.org/10.1021/acs.inorgchem.8b01574.

[56] X. Zhang, J. Wang, X. Ji, Y. Sui, F. Wei, J. Qi, Q. Meng, Y. Ren, Y. He, Nickel/cobalt bimetallic metal-organic frameworks ultrathin nanosheets with enhanced performance for supercapacitors, J. Alloy. Compd. 825 (2020) 154069, https://doi.org/10.1016/j.jallcom.2020.154069.

[57] D. Acharya, I. Pathak, B. Dahal, P.C. Lohani, R.M. Bhattarai, A. Muthurasu, T. Kim, T.H. Ko, K. Chhetri, H.Y. Kim, Immoderate nanoarchitectures of bimetallic MOF derived Ni–Fe–O/NPC on porous carbon nanofibers as freestanding electrode for asymmetric supercapacitors, Carbon N. Y 201 (2023) 12–23, https://doi.org/10.1016/j.carbon.2022.08.091.

[58] K. Chhetri, T. Kim, D. Acharya, A. Muthurasu, B. Dahal, R.M. Bhattarai, P. C. Lohani, I. Pathak, S. Ji, T.H. Ko, H.Y. Kim, Hollow carbon nanofibers with inside-outside decoration of bi-metallic MOF derived Ni-Fe phosphides as electrode materials for asymmetric supercapacitors, Chem. Eng. J. 450 (2022) 138363, https://doi.org/10.1016/j.cej.2022.138363.

[59] P.P. Sun, Y.H. Zhang, H. Shi, F.N. Shi, Controllable one step electrochemical synthesis of PANI encapsulating 3d-4f bimetal MOFs heterostructures as electrode materials for high-performance supercapacitors, Chem. Eng. J. 427 (2022) 130836, https://doi.org/10.1016/j.cej.2021.130836.

[60] G. Sahoo, H.S. Jeong, S.R. Polaki, S.M. Jeong, Vertical graphene nanosheets as interface current-collector for enhanced charge-storage kinetics of bimetallic MOF nano-rods and asymmetric solid-state supercapacitors, J. Energy Storage 68 (2023) 107824, https://doi.org/10.1016/j.est.2023.107824.

[61] S.B. Dhavale, V.L. Patil, S.S. Patil, R.P. Dhavale, H.H. Park, T. Kim, P.S. Patil, Nanostructured NiCo2O4 embedded on biowaste derived hierarchical porous activated carbon for high performance symmetric and asymmetric supercapacitor device, J. Energy Storage 72 (2023) 108820, https://doi.org/10.1016/j.est.2023.108820.

[62] S.S. Shalini, R. Balamurugan, S. Velmathi, A.C. Bose, Systematic investigation on the electrochemical performance of pristine silver metal-organic framework as the efficient electrode material for supercapacitor application, Energy Fuels 36 (2022) 7104–7114, https://doi.org/10.1021/acs.energyfuels.2c01034.

[63] G.M. Kalu-Uka, S. Kumar, A.C. Kalu-Uka, S. Vikram, G.O. Ihekweme, N. Ranjan, E. N. Anosike-Francis, G. Prajapati, A. Nduba, A.P. Onwualu, S. Kumar, Production of

activated carbon electrode for energy storage application in supercapacitors via KOH activation of waste termite biomass, Waste Biomass. Valoriz. 13 (2022) 2689–2704, https://doi.org/10.1007/s12649-022-01680-6.

[64] F. Dai, X. Wang, S. Zheng, J. Sun, Z. Huang, B. Xu, L. Fan, R. Wang, D. Sun, Z. S. Wu, Toward high-performance and flexible all-solid-state micro-supercapacitors: MOF bulk vs. MOF nanosheets, Chem. Eng. J. 413 (2021) 127520, https://doi.org/10.1016/j.cej.2020.127520.

[65] L. Wang, Y. Yang, B. Wang, C. Duan, J. Li, L. Zheng, J. Li, Z. Yin, Bifunctional three-dimensional self-supporting multistage structure CC@MOF-74(NiO)@NiCo LDH electrode for supercapacitors and non-enzymatic glucose sensors, J. Alloy. Compd. 885 (2021) 160899, https://doi.org/10.1016/j.jallcom.2021.160899.

[66] Q. Yu, J. Gong, W. Kong, Y. Long, J. Chen, L. Pu, H. Zhang, Y. Dai, Preparation of NiAl LDH@Mn3O4@Co-MOF ternary composites using MOFs as a framework for high-performance asymmetric supercapacitors, Electrochim. Acta 428 (2022) 140913, https://doi.org/10.1016/j.electacta.2022.140913.

[67] Q. Bi, Q. Ma, K. Tao, L. Han, Hierarchical Core–shell 2D MOF Nanosheet Hybrid Arrays for High-performance Hybrid Supercapacitors, (2021) 8179–8188. https://doi.org/10.1039/d1dt00866h.

[68] F. Boorboor Ajdari, M. Dashti Najafi, M. Izadpanah Ostad, H. reza Naderi, M. Niknam Shahrak, E. Kowsari, S. Ramakrishna, A symmetric ZnO-ZIF8//Mo-ZIF8 supercapacitor and comparing with electrochemical of Pt, Au, and Cu decorated ZIF-8 electrodes, J. Mol. Liq. 333 (2021) 116007, https://doi.org/10.1016/j.molliq.2021.116007.

[69] L. Sun, Y. Liu, M. Yan, Q. Yang, X. Liu, W. Shi, Lewis acid etched NixCo1-xSe2 derived from ZIF-L on CoO nanowires for hybrid-supercapacitors, Chem. Eng. J. 431 (2022), https://doi.org/10.1016/j.cej.2021.133472.

[70] Z. Ma, J. Li, R. Ma, J. He, X. Song, Y. Yu, Y. Quan, G. Wang, The methodologically obtained derivative of ZIF-67 metal-organic frameworks present impressive supercapacitor performance, N. J. Chem. 46 (2022) 7230–7241, https://doi.org/10.1039/d2nj00646d.

[71] A.R. Mule, B. Ramulu, J.S. Yu, Prussian-blue analogue-derived hollow structured Co3S4/CuS2/NiS2 nanocubes as an advanced battery-type electrode material for high-performance hybrid supercapacitors, Small 18 (2022) 1–12, https://doi.org/10.1002/smll.202105185.

[72] J. Yan, Z. Fan, T. Wei, W. Qian, M. Zhang, F. Wei, Fast and reversible surface redox reaction of graphene-MnO2 composites as supercapacitor electrodes, Carbon N. Y 48 (2010) 3825–3833, https://doi.org/10.1016/j.carbon.2010.06.047.

[73] F. Tang, Q. Xiao, W. Zhu, G. Pezzotti, J. Zhu, Facile syntheses of Fe2O3-rGO and NiCo-LDH-rGO nanocomposites for high-performance electrochemical capacitors, J. Colloid Interface Sci. 634 (2023) 357–368, https://doi.org/10.1016/j.jcis.2022.12.053.

[74] H. Zhang, Y. Xie, S. Yang, X. Gao, H. Bai, F. Yao, H. Yue, NiCo2S4 nanocone arrays on three-dimensional graphene with small hole diameters for asymmetric supercapacitor, J. Alloy. Compd. 968 (2023) 171694, https://doi.org/10.1016/j.jallcom.2023.171694.

[75] Z. Zhou, Y. Li, Q.G. Wang, J. Yu, Health indicators identification of lithium-ion battery from electrochemical impedance spectroscopy using geometric analysis, IEEE Trans. Instrum. Meas. 72 (2023) 1–9, https://doi.org/10.1109/TIM.2023.3272401.

[76] J. Sun, Y. Liu, Unique constant phase element behavior of the electrolyte–graphene interface, Nanomaterials 9 (2019), https://doi.org/10.3390/nano9070923.

[77] Z. Ebrahimi, M. Rad, V. Safarifard, M. Moradi, Solvent-assisted ligand exchange as a post-synthetic surface modification approach of Zn-based (ZIF-7, ZIF-8) and Co-based (ZIF-9, ZIF-67) zeolitic frameworks for energy storage application, J. Mol. Liq. 364 (2022) 120018, https://doi.org/10.1016/j.molliq.2022.120018.

[78] I.S. Ike, I. Sigalas, S. Iyuke, Understanding performance limitation and suppression of leakage current or self-discharge in electrochemical capacitors: a review, Phys. Chem. Chem. Phys. 18 (2015) 661–680, https://doi.org/10.1039/c5cp05459a.

[79] A. Kumaravel, S. Sathyamoorthi, High-voltage aqueous electrolyte–based supercapacitor using biocarbon derived from Pedalium murex waste with commercial-level areal mass loading, Ionics 30 (2024) 4143–4153, https://doi.org/10.1007/s11581-024-05538-w.

[80] M.N. Rantho, M.J. Madito, F.O. Ochai-Ejeh, N. Manyala, Asymmetric supercapacitor based on vanadium disulfide nanosheets as a cathode and carbonized iron cations adsorbed onto polyaniline as an anode, Electrochim. Acta 260 (2018) 11–23, https://doi.org/10.1016/j.electacta.2017.11.074.

[81] B. Pandit, B.R. Sankapal, P.M. Koinkar, Novel chemical route for CeO 2 /MWCNTs composite towards highly bendable solid-state supercapacitor device, Sci. Rep. 9 (2019) 1–14, https://doi.org/10.1038/s41598-019-42301-y.

[82] A. Singh, A.K. Ojha, Orange peel derived activated carbon for supercapacitor electrode material, J. Mater. Sci. Mater. Electron. 34 (11) (2023) 1, https://doi.org/10.1007/s10854-023-10418-6.